

ARTICLE

Received 16 Dec 2014 | Accepted 19 May 2015 | Published 20 Jul 2015

DOI: 10.1038/ncomms8568

OPEN

Quantitative X-ray phase-contrast microtomography from a compact laser-driven betatron source

J. Wenz^{1,2}, S. Schleede³, K. Khrennikov^{1,2}, M. Bech^{3,4}, P. Thibault^{3,5}, M. Heigoldt^{1,2}, F. Pfeiffer³ & S. Karsch^{1,2}

X-ray phase-contrast imaging has recently led to a revolution in resolving power and tissue contrast in biomedical imaging, microscopy and materials science. The necessary high spatial coherence is currently provided by either large-scale synchrotron facilities with limited beamtime access or by microfocus X-ray tubes with rather limited flux. X-rays radiated by relativistic electrons driven by well-controlled high-power lasers offer a promising route to a proliferation of this powerful imaging technology. A laser-driven plasma wave accelerates and wiggles electrons, giving rise to a brilliant keV X-ray emission. This so-called betatron radiation is emitted in a collimated beam with excellent spatial coherence and remarkable spectral stability. Here we present a phase-contrast microtomogram of a biological sample using betatron X-rays. Comprehensive source characterization enables the reconstruction of absolute electron densities. Our results suggest that laser-based X-ray technology offers the potential for filling the large performance gap between synchrotron- and current X-ray tube-based sources.

¹Ludwig-Maximilians-Universität München, Fakultät für Physik, Am Coulombwall 1, Garching 85748, Germany. ²MPI für Quantenoptik, Abteilung für Attosekundenphysik, Hans-Kopfermann-Str. 1, Garching 85748, Germany. ³Lehrstuhl für Biomedizinische Physik, Physik-Department & Institut für Medizintechnik, Technische Universität München, Garching 85748, Germany. ⁴Department of Medical Radiation Physics, Clinical Sciences, Lund University, Barngatan 2:B, Lund 22185, Sweden. ⁵Department of Physics and Astronomy, University College London, Gower street, London WC1E 6BT, UK. Correspondence and requests for materials should be addressed to S.K. (email: stefan.karsch@mpq.mpg.de).

Since the discovery of X-ray radiation and its powerful imaging capabilities by Röntgen, X-rays have become a part of our daily life in medicine, industry and research. The conventional technique of absorption imaging utilizes the large absorption variations of X-rays in matter (that is, the imaginary part β of the refractive index $n = 1 - \delta + i\beta$) of different thickness and composition, limiting its usefulness to structures with high absorption gradients. However, the real part of the refractive index δ leads to phase variations of the X-rays depending on the sample's electron density. The latter can be explored with much higher sensitivity by phase-contrast techniques^{1,2}, which are far superior to conventional radiography for detecting structures in soft tissue with its rather homogeneous absorption profile. It is thus ideally suited for three-dimensional (3D) investigations of (pathologic) tissue biopsies in medical research and diagnostics³, but also finds applications in materials science. Computed tomography using phase-contrast images taken from different perspectives can provide the full 3D structure of the object with high resolution and enhanced contrast. Phase-contrast imaging is complementary to coherent diffractive imaging⁴, which is employed for tomographic reconstruction in the far field.

Phase-contrast imaging can be implemented by free-space propagation (also known as in-line holography)⁵, crystal analyser-based² and crystal^{3,6} or grating⁷ interferometer-based techniques. For microscopy applications with micron-scale resolution, propagation-based phase-contrast imaging is the method of choice. It relies neither on additional X-ray optics, nor on substantial temporal coherence of the source. The only requirement is that the transverse coherence length, given by $l_t = \lambda \cdot R/\sigma$ is larger than $\sqrt{\lambda D}/(2\sqrt{2}) \cong O(1 - 10 \mu\text{m})$ ⁸. Here λ is the wavelength, R is the source–detector distance, σ is the source size and $D = d \cdot l/(d + l)$ the defocusing distance with l as source–sample and d sample–detector distances. This is met by third-generation synchrotrons, but their size and cost prevent their proliferation in hospitals and research institutions. Microfocus X-ray tubes provide the desired spatial coherence but suffer from a modest X-ray flux, implying lengthy exposure times. To spark off widespread application of this powerful technique, a compact high-brilliance source is needed.

Laser-wakefield acceleration of electrons⁹ (LWFA; see Methods) has already been studied as a possible future alternative. LWFA of electron beams exhibit transverse emittances comparable to the best conventional linear accelerators and bunch durations of ~ 5 fs full-width at half-maximum (FWHM)^{10,11}, rendering them unique among compact sources. During the acceleration process the electrons are also wiggled transversely by the strong radial fields of the plasma wave, causing them to emit a forward-directed, incoherent X-ray beam, referred to as betatron radiation^{12–14} (see Methods).

Recent proof-of-principle experiments demonstrated the potential of laser-driven betatron sources for recording single-shot X-ray phase-contrast images based on the free-space propagation technique¹⁵. Here we demonstrate that this type of source—even at this early stage of development—can be readily used for real-world applications. Due to advances in LWFA stability by using a turbulence-free steady-state gas flow target^{16,17}, we are able to produce electron bunches with high charge (400 pC) and low fluctuations in absolute charge (30%) and in cut-off energy (10%) for continuous operation of several hours. We also show experimentally in this work that the spectral shape of the betatron radiation is largely insensitive to the electron spectra fluctuation. This leads to the production of a high-flux X-ray beam with remarkable spectral stability ideally suited for multiexposure imaging. Using these beams we were for the first time able to record and quantitatively reconstruct a phase tomogram of a complex object. As an illustrative example, we

chose a dried insect (*Chrysoperia carnea*, green lacewing). We achieved this by evaluating a set of 1,487 single-shot phase-contrast images taken from various angles (Supplementary Movie 1). The microradiography images features a field of view of $7.5 \times 6.9 \text{ mm}^2$ and a resolution of $6 \mu\text{m}$, limited by the CCD (charge-coupled device) area and pixel size, respectively. For quantitative reconstruction of the tomogram¹⁸ from these images, we performed a careful characterization of the X-ray source in terms of its transverse dimensions and spectrum, which is essential for the reconstruction of the absolute electron densities within the object of interest¹⁹.

Results

Source characterization. In the experiment, intense short laser pulses were focused at the entrance of a hydrogen-filled gas cell (see Fig. 1 and Methods). For our pulse parameters the highest electron energies with a peak at 400 MeV, lowest divergences (1.3 ± 0.2 mrad) FWHM and moderate charge (50 pC) were produced at plasma electron densities of $5 \times 10^{18} \text{ cm}^{-3}$, created from laser-induced field ionization of the target gas.

The betatron motion leads to the emission of well-collimated X-ray beams with a spectrum peaked at 4.9 keV, measured by their transmission through a stack of filters²⁰. However, when the plasma density is increased to $1.1 \times 10^{19} \text{ cm}^{-3}$, the electron energy drops to 200 MeV and their divergence increases up to 5 mrad, along with a substantial increase of electron beam charge to 400 pC. Now the X-ray beam divergence triples from (2.3 ± 0.2 mrad) to (6.0 ± 1.1 mrad) and the photon fluence increases by more than an order of magnitude. The energy spectrum stays roughly constant, partly because higher wiggling fields in the dense plasma offset the lower electron energies. The increase in photon number results from the marked increase of trapping efficiency at higher densities. It is evident from Fig. 2a that despite large shot-to-shot variations in the electron spectrum in this high-density regime, the X-ray spectrum is remarkably stable, a behaviour not reported before. We attribute this to the fixed low-energy cutoff of the aluminium laser blocking filter (see Fig. 1 and Methods) on one hand and to the incoherent superposition of emission from many electrons with a broad spectrum on the other hand. This betatron-optimized regime results in the emission of 1.2×10^9 photons msr^{-1} per shot ($\pm 20\%$) above 1 keV, at the position of the object.

The source size was derived from the Fresnel diffraction pattern of an object in the X-ray beam, as shown in Fig. 2b. Comparison of a modelled diffraction pattern with the data yields a source size of ($1.8 \pm 0.1 \mu\text{m}$ r.m.s.(root mean square)). Assuming pulse durations of 5 fs as suggested by numerical studies, recent reports^{10,11} and our own yet unpublished measurements, the source exhibits a peak brilliance of 2×10^{22} photons $\text{s}^{-1} \text{ mm}^{-2} \text{ mrad}^{-2}$ within a relative spectral bandwidth of 0.1% at the position of our sample. In the current proof-of-principle experiment, the average brilliance and photon flux density at the sample was limited to 1×10^7 photons $\text{s}^{-1} \text{ mm}^{-2} \text{ mrad}^{-2}$ within a relative spectral bandwidth of 0.1% and 2×10^7 photons $\text{s}^{-1} \text{ cm}^{-2}$, respectively, owing to a shot rate of 0.1 Hz due to gas load in the chamber and data acquisition limitations. An optimized pumping design and improved data acquisition permitting the full 5-Hz shot rate of the laser would improve these figures by a factor of 50 and yield few-minute scan times.

The scalability of the photon energy depends on the electron energy, the plasma density and the wiggler strength parameter, which in LWFA are all interlinked⁹. Clever target engineering, that is, separating acceleration and radiation zone, off-axis injection²¹ or laser-betatron resonance effects²² may strongly

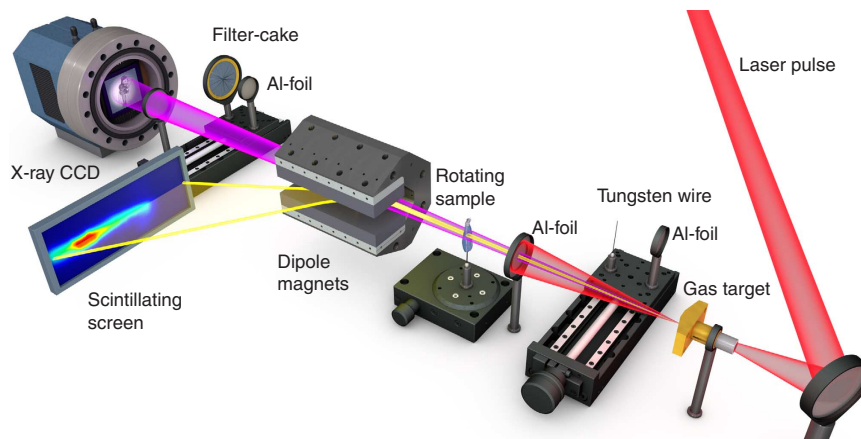


Figure 1 | Experimental setup. The laser pulse (1.6 J, 28 fs, 60 TW) (red) is focused by a $F/16$ off-axis parabola to a $22\text{-}\mu\text{m}$ diameter spot size on the entrance of a 6-mm long gas cell with an plasma electron density of $n_p = 1.1 \times 10^{19} \text{ cm}^{-3}$. The residual laser light is blocked by a $10\text{-}\mu\text{m}$ thick aluminium foil in front of the detector. Dipole magnets deflect the accelerated electrons (yellow) away from the laser axis onto a scintillating screen (LANEX). The X-ray beam (pink) transmitted through the foil is recorded by a cooled back-illuminated X-ray CCD with $22.5\text{-}\mu\text{m}^2$ pixels. The tomogram was acquired in the experimental configuration as shown. The thickness of the Al-foil in front of the sample was $20\text{ }\mu\text{m}$ to protect it from the laser light during the scan. The ‘Al-cake’ and wire-arrangement each protected by an Al foil of $10\text{-}\mu\text{m}$ thickness can be inserted into the X-ray beam for spectral and source size characterization. The Al foil of $10\text{-}\mu\text{m}$ thickness in front of the CCD was present during whole experiment.

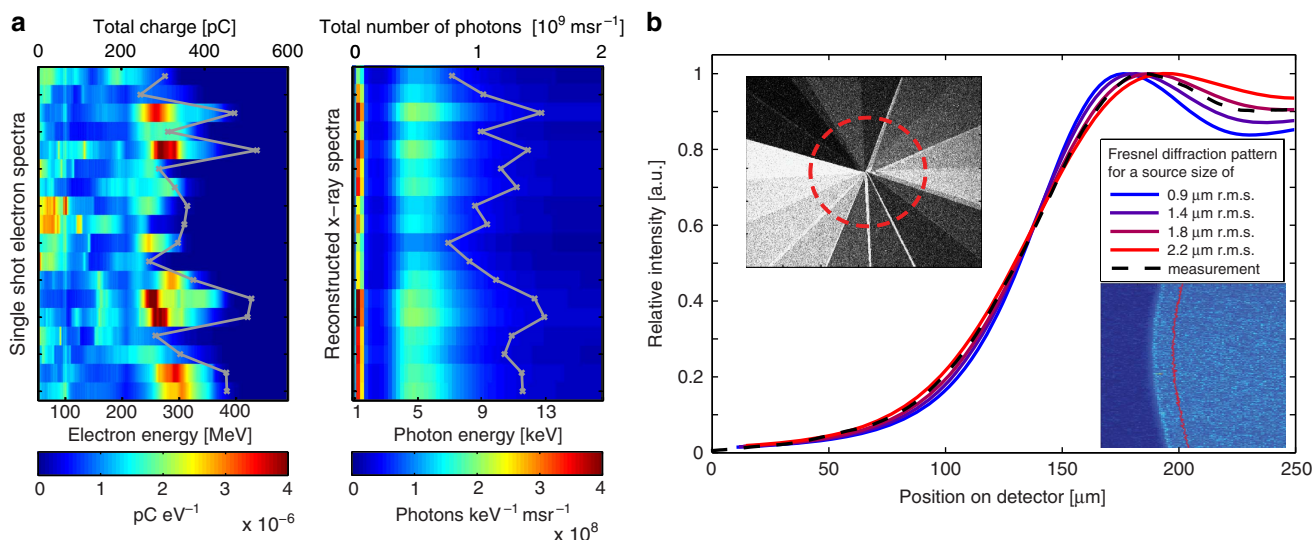


Figure 2 | Characterization of the betatron source. (a) Electron and corresponding X-ray spectra as seen by the sample for 18 individual laser shots. The X-ray spectra were reconstructed from the transmission signal of the filter cake with overall thicknesses ranging from 20 to $630\text{ }\mu\text{m}$ (see left inset in **b**). Inside the red circle, corresponding to $(1.35 \times 10^{-2}) \text{ msr}$, $(1.6 \pm 0.3) \times 10^7$ photons are detected and analysed for their energy. Even for large electron energy fluctuations, the X-ray spectral shape is remarkably stable. (b) Source size measurement: A comparison of the measured intensity distribution integrated along a $100\text{-}\mu\text{m}$ thick tungsten wire (right inset) and the modelled intensity distribution for a Gaussian source spot, taking into account the spectra in **a**, reveal a best value of $1.8\text{ }\mu\text{m}$ r.m.s.

enhance the betatron amplitude and hence the critical energy. In ref. 22, a 20-keV X-ray spectrum with a tail to 1 MeV was achieved with laser pulses containing only three times more energy. The shot-to-shot stability of our X-ray source is excellent for a laser-driven process, yielding $>10^7$ photons per shot in $>99\%$ of the laser shots in the tomographic scan, with low fluctuations of the X-ray spectrum (see Fig. 2a), and a photon number constant to within $\pm 20\%$ r.m.s., making it suitable for multiexposure tomography.

Tomography. For the tomography scan the object was placed on a rotating mount into the X-ray beam (see Fig. 1). Although a dried sample exhibits different electron densities compared with a

fresh tissue, it was chosen for technical simplicity for this proof-of-concept experiment. Its ability to be put within the vacuum chamber avoided unnecessary intermediate air propagation (as the cooled CCD chip needs to be evacuated), and consequently unnecessary transmission losses in X-Ray windows.

The raw phase-contrast images recorded on the CCD exhibit the so-called edge-enhancement effect (Fig. 3a), which is inherent to propagation-based phase-contrast imaging⁸ in the Fresnel diffraction regime. No optical elements between the source and the detector are used, but the wave propagates sufficiently far beyond the sample (1.99 m) for Fresnel diffraction to occur. The edge-enhanced image is useful by itself for visual inspection when high-resolution features with poor absorption contrast (Fig. 3a) are of particular interest. However, propagation-induced

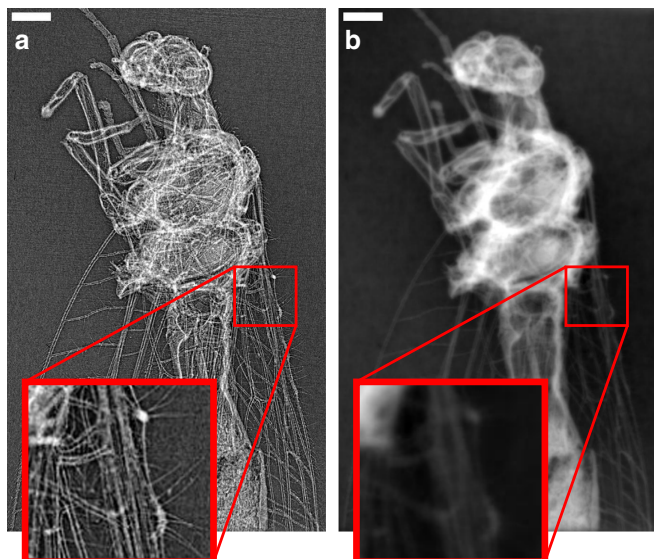


Figure 3 | Lacewing insect (*Chrysoperia carnea*), imaged with AI-filtered betatron X-ray spectrum. (a) The image shows a selected single-shot radiograph dominated by X-ray in-line phase contrast. Small details are highlighted due to the strong edge enhancement effect (see insets of magnified sections). (b) The corresponding quantitative phase map was retrieved using a single-material constraint. A series of these maps is used for the reconstruction of the insect as shown in Figs 4 and 5. Scale bar, 0.5 mm (white).

intensity fringes of a pure phase object are not a direct measure of the phase shift but rather the Laplacian of the phase front⁵. A reconstruction of raw phase projections will thus only yield grey level variations at material interfaces (Fig. 4a). Due to the missing link of reconstructed contrast to material properties, a quantitative analysis and automatic segmentation via thresholding is not possible.

In absorption tomography, projections of the linear absorption coefficient along the beam are directly obtained from the logarithm of the recorded intensity. The subsequent reconstruction exhibits area contrast with grey values directly related to material properties of the sample under investigation. Starting from diffracted intensity measurements at a certain propagation distance, phase-retrieval algorithms are employed to create line projection images of the refractive index decrement δ (phase maps, see Methods). The transport-of-intensity equation (TIE) relates the edge-enhanced image measured at the detector to the phase distribution at the exit plane of the sample. As we only used one propagation distance we employed a single-material constraint to solve the TIE and retrieve phase maps of the insect (Fig. 3b; see Methods).

As the retrieved phase map is directly related to the integrated decrement δ of the index of refraction, the reconstruction yields information on electron density distribution in the sample. Before reconstruction, the 360 projections taken over 360° were each averaged over four subsequent laser shots and binned by a factor of two in both image dimensions to yield an artifact-free reconstruction (see Methods). Standard filtered back projection was used to reconstruct the transverse slices shown in Fig. 4b,c. The reconstruction reveals a distinct contrast between insect and background, allowing segmentation via simple thresholding. Additional TEM measurement of the insect's leg revealed that the reconstructed electron densities are in good agreement—under the consideration of the resolution of our setup—with the expected electron densities for chitin (see Supplementary Note 1).

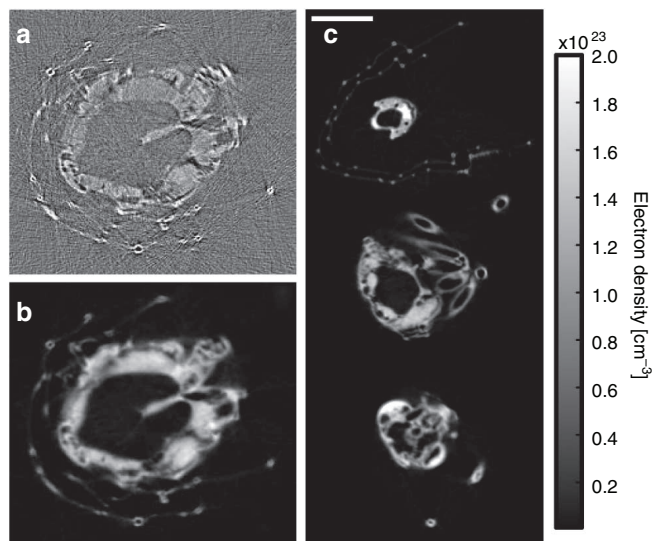


Figure 4 | Transverse slices of the sample. (a) A reconstructed transverse slice of the lacewing without phase-retrieval (that is, using raw phase-contrast images as in Fig. 3a) highlights material boundaries but does not allow for a quantitative analysis. (b) The same transverse slice reconstructed after phase retrieval, using phase images as in Fig. 3b. (c) Reconstructed transverse slices as in (b) with grey values representing electron density values. The reconstruction exhibits good area contrast allowing for volume rendering and segmentation as shown in Fig. 5. Electron density scale applies to subfigures (b) and (c). Scale bar, 1 mm (white).

A 3D rendering of the sample is presented (see Fig. 5 and Supplementary Movie 2), including sectioning planes of the 3D volume with grey levels corresponding to electron density.

Discussion

This result demonstrates that laser-driven X-ray sources have reached the verge of practical usefulness for application-driven research. If further progress regarding mean photon flux can be made, laser-driven sources due to their compactness, relatively low cost and high peak brilliance might become valuable tools for university-scale research and medical application, in particular early detection of tumours with low-dose diagnostics. Here difficulties in interpreting conventional radiograms and the continuous increase in cancer probability (due to prolonged life) have led to substantial interest of the possible improvements offered by phase-contrast imaging. These phase-contrast images provide higher contrast, especially, when normal and malignant tissue exhibit almost the same attenuation coefficient. Such studies already performed on small animals and human tissue samples proved an enhanced contrast and better tumour visibility^{23,24} as long as a high resolution in electron densities is provided.

On the basis of the distribution of the grey values in the background (void) of our reconstructed sample (Fig. 4) we can estimate a conservative limit for our measurement sensitivity of the electron density to $0.1 \times 10^{23} \text{ cm}^{-3}$. This resolution would already be sufficient to detect malignant tissue (assuming a mass density of 1.01 g cm^{-3} and corresponding electron density due to its chemical composition²⁵ of $3.28 \times 10^{23} \text{ cm}^{-3}$) within the lungs²⁶ (mass density of 0.38 g cm^{-3} and an electron density of $1.26 \times 10^{23} \text{ cm}^{-3}$) or even in the brain (mass density of 1.05 g cm^{-3} with an electron density of $3.49 \times 10^{23} \text{ cm}^{-3}$). If the source energy can be pushed into the tens of keV range, as recent results suggest²⁷, such laser-based sources could be an

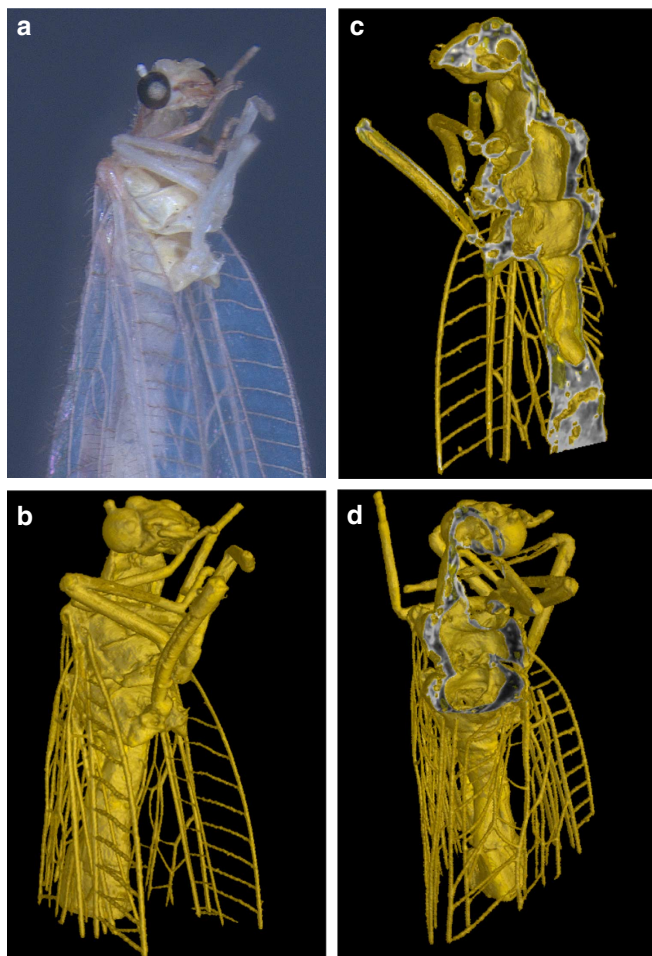


Figure 5 | Volume rendering. (a) Photograph of the sample. (b) 3D rendering of the sample, imaged with Al-filtered betatron X-ray spectrum. (c,d) Cutting planes of the 3D volume are shown with their grey levels corresponding to electron density distribution in the sample.

alternative to the conventional radiography with superior resolution avoiding invasive surgery and time-consuming histology and improvement for image-guided radiation therapy, where detection and accurate positioning of the target tissue volumes is required²⁸ (and references therein).

Further applications, may not only exploit the imaging capabilities of such a table top X-ray source, but also benefit from its ultrashort nature. Ultrafast structural X-ray science would be a good example including time-resolved pump probe X-ray absorption^{29,30} or diffraction^{31,32} experiments resolving fast atomic and molecular motion. Here the unique combination of broadband radiation, intrinsically perfect synchronization to a laser pulse and few femtoseconds pulse duration would offer a crucial advantage.

In view of the ongoing dynamic evolution in high-energy, high-repetition rate laser technology^{33,34} aiming to scale multi-TW lasers to kHz and beyond, average fluences approaching current state-of-the-art compact synchrotron sources are expected to become available in the near future. This might help proliferation of biomedical X-ray diagnostics, X-ray microscopy and non-destructive industrial testing for static—as demonstrated here by a microtomogram of a biological sample—and in particular time-resolved imaging with femtosecond resolution would definitely further benefit from the development.

Methods

Laser-wakefield acceleration. The experiments were performed using the ATLAS Ti:Sapphire laser at the MPI for Quantum Optics. It occupies a table area of $\sim 15\text{ m}^2$, and delivers 1.6 J energy, 28 fs duration (60 TW) laser pulses, centred at 800 nm wavelength. They are focused onto the entrance of a Hydrogen-filled gas cell by an off-axis parabolic mirror ($f = 1.5\text{ m}$, $F/20$) to a spot size of $22\text{ }\mu\text{m}$ FWHM. This corresponds to a vacuum peak intensity of $1 \times 10^{19}\text{ W cm}^{-2}$. At these intensities, the hydrogen is fully ionized and the laser propagates through plasma. Its strong ponderomotive force drives a plasma wave with frequency $\omega_p = \sqrt{\frac{4\pi n_e e^2}{m_e \epsilon_0}}$. Here n_e , e and m_e are the density, charge and rest mass of the plasma electrons, and ϵ_0 is the vacuum permittivity. The wave phase velocity matches the laser group velocity, so that in the frame of the laser pulse, the plasma wave constitutes a co-moving accelerating field. Electrons from the plasma are trapped into this wave by wave-breaking and accelerated to relativistic energies around 200–400 MeV, depending on the electron density. A magnet deflects the electron beam according to energy onto a scintillating screen (see Fig. 1). From the position and brightness on the screen the energy, divergence and charge of the electron bunch can be deduced³⁵.

Betatron radiation. The plasma wavelength $\lambda_p = \frac{2\pi c}{\omega_p}$ confines the wakefield to a radius of $\sim 10\text{ }\mu\text{m}$, causing strong radial fields that force the electrons into anharmonic transverse betatron oscillations at a frequency $\omega_\beta = \frac{\omega_p}{\sqrt{2\gamma}}$ during acceleration. Here, γ is the relativistic factor of the electron beam. The strong radial fields lead to large angular excursions, while keeping the beam size within a few microns, triggering the emission of high harmonics of ω_β in a co-moving frame. ω_β varies during acceleration, causing incoherent emission. In the laboratory frame, the radiation is relativistically boosted to the X-ray regime and merges into a synchrotron-like continuum, described by a critical energy $E_{\text{crit}} = \frac{3\hbar K \gamma^2 \omega_\beta}{2\pi}$. Here K is the wiggler parameter defined through $K \approx \gamma \theta^3$, where θ is the opening angle of the emitted radiation. For our experimental conditions, even a small off-axis distance of $1\text{ }\mu\text{m}$ corresponds to a wiggler parameter on the order of 10, leading to high harmonic orders.

For the spectrum and source size measurements, the X-rays are freely propagating from the source to an Andor model DO432 BN-DD back-illuminated CCD detector at a distance of 3.26 m. The on-axis laser light is blocked behind the source by two 10- μm thick Al-foils which are transparent for radiation above 1 keV. A filter cake with different material thicknesses for spectrum characterization and a Tungsten wire for source size analysis can be moved into the beam. For the tomography studies the sample is mounted $l = 0.73\text{ m}$ from the source, $d = 1.99\text{ m}$ in front of the detector, yielding a $3.7 \times$ magnification.

Modelling of Fresnel diffraction. The source size was derived by analysing the Fresnel diffraction pattern from a tungsten wire backlit by the X-ray beam. The measured edge diffraction on the detector from a 100- μm thick Tungsten wire (26-cm behind the source) is shown in the inset of Fig. 2b, and was compared to modelled distributions for various source sizes. They were obtained by summing up the Fresnel diffraction from a knife edge, as described in for example, Born and Wolf³⁶ for all energy bins of the incident spectrum weighted by the CCD response. The beam, showing a Gaussian shape on the CCD chip, was assumed to be Gaussian at the origin. The result for different source sizes is shown in the inset of Fig. 2b. The information about the source size is completely indicated by the first overshoot of the profile. To improve the signal to noise ratio we have vertically summed up the profiles, taking into account the curvature of the wire by a cross-correlation between different rows. Our analysis yields a best fit for a source size of $(1.8 \pm 0.1\text{ }\mu\text{m r.m.s.})$.

Phase retrieval. The TIE directly relates the phase distribution in the planes orthogonal to the optical axis to the propagation of the wavefront intensity of the beam. A variety of phase-retrieval algorithms, which solve the TIE, have been proposed, differing in raw data input needed (for example, multiple sample to detector distances) and additional constraints on sample material properties³⁷. We use a single-distance quantitative phase-retrieval method that does not require the sample to show negligible absorption¹⁹. It employs a single-material constraint corresponding to a fixed d/β ratio representing the sample's main chemical component. If this assumption is justified and the sample exhibits comparably weak absorption such as in our case, this approach allows for a quantitative reconstruction of electron density values in the sample as shown in³⁸. The projected thickness of the sample which is directly related to the phase shift imposed onto the wavefront via $\varphi(\mathbf{r}) = -2\pi/\lambda_{\text{mean}} \delta_{\text{poly}} T(\mathbf{r})$, can be retrieved by using the following equation¹⁹:

$$T(\mathbf{r}) = -\frac{1}{\mu_{\text{poly}}} \ln \left(\mathcal{F}^{-1} \left\{ \frac{\mathcal{F}(I(M\mathbf{r}))}{I_0} \frac{R \delta_{\text{poly}}}{1 + \frac{R \delta_{\text{poly}}}{M \mu_{\text{poly}} |\mathbf{k}|^2}} \right\} \right). \quad (1)$$

Here T is the retrieved thickness of the sample, \mathbf{r} are the transverse coordinates, \mathbf{k} are the Fourier space coordinates, I is the measured intensity, I_0 is the uniform intensity of the incident radiation, M is the magnification of the image, R is the distance from the sample to the detector and μ_{poly} and δ_{poly} are the material-dependent linear absorption coefficient and refractive index decrement,

respectively. In the case of a polychromatic X-ray spectrum the most accurate phase-retrieval results are achieved through the calculation of effective μ and δ values. We assume the main chemical composition present in the dried insect to be Chitin ($C_8H_{13}NO_5$). Values of $\mu_{\text{poly}} = 70.15 \text{ cm}^{-1}$ and $\delta_{\text{poly}} = 1.38 \times 10^{-5}$ were calculated from reconstructed X-ray spectra (see Fig. 2a), tabulated $\delta(E)$ and $\beta(E)$ values at a density of $\rho = 2.2 \text{ g cm}^{-3}$ ³⁹, and the known detector response function⁴⁰. The phase map as depicted in Fig. 3b) was reconstructed using equation (1) with values of $R = 199 \text{ cm}$, $M = 3.7$ and a mean energy as seen by the detector of $E_{\text{mean}} = 8.8 \text{ keV}$ ($\lambda_{\text{mean}} = 1.4 \text{ \AA}$). This mean energy seen by the detector is different from the spectral peak of the source as it takes into account the additional Al-filter and spectral weighting.

Treatment of raw images. The fluctuations of the X-ray point of origin (12 μm r.m.s. vertical, 18 μm r.m.s. horizontal) are caused by shot-to-shot laser pointing fluctuations. To correct for these, before reconstruction all images were registered using normalized cross-correlation. The shape of the correlation surface is assumed to fit two orthogonal parabolic curves. Sub-pixel registration accuracy is obtained by fitting a paraboloid to the 3×3 pixel vicinity of the maximum value of the cross-correlation matrix. Sub-pixel shifting is performed in Fourier space. To account for the Gaussian intensity profile of the X-ray beam the sample is masked out using an edge detection filter and images are background corrected by subtracting a second order polynomial. The vertical alignment of the tomography scan is performed using cross-correlation of integrated pixel values perpendicular to the tomography axis. Horizontal alignment was performed manually.

References

- Davis, T. J., Gao, D., Gureyev, T. E., Stevenson, A. W. & Wilkins, S. W. Phase-contrast imaging of weakly absorbing materials using hard X-rays. *Nature* **373**, 595–598 (1995).
- Ingal, V. N. & Beliaevskaya, E. A. X-ray plane-wave topography observation of the phase contrast from a non-crystalline object. *J. Phys. D Appl. Phys.* **28**, 2314–2317 (1995).
- Momose, A., Takeda, T., Itai, Y. & Hirano, K. Phase-contrast X-ray computed tomography for observing biological soft tissues. *Nat. Med.* **2**, 473–475 (1996).
- Williams, G. *et al.* Fresnel Coherent Diffractive Imaging. *Phys. Rev. Lett.* **97**, 025506 (2006).
- Wilkins, S. W., Gureyev, T. E., Gao, D., Pogany, A. & Stevenson, A. W. Phase-contrast imaging using polychromatic hard X-rays. *Nature* **384**, 335–338 (1996).
- Bonse, U. & Hart, M. An X-ray interferometer. *Appl. Phys. Lett.* **6**, 155–156 (1965).
- Pfeiffer, F., Weitkamp, T., Bunk, O. & David, C. Phase retrieval and differential phase-contrast imaging with low-brilliance X-ray sources. *Nat. Phys.* **2**, 258–261 (2006).
- Cloetens, P. *et al.* Observation of microstructure and damage in materials by phase sensitive radiography and tomography. *J. Appl. Phys.* **81**, 5878–5886 (1997).
- Esarey, E., Schroeder, C. & Leemans, W. Physics of laser-driven plasma-based electron accelerators. *Rev. Mod. Phys.* **81**, 1229–1285 (2009).
- Buck, A. *et al.* Real-time observation of laser-driven electron acceleration. *Nat. Phys.* **7**, 543–548 (2011).
- Lundh, O. *et al.* Few femtosecond, few kiloampere electron bunch produced by a laser-plasma accelerator. *Nat. Phys.* **7**, 219–222 (2011).
- Rousse, A. *et al.* Production of a keV X-Ray beam from synchrotron radiation in relativistic laser-plasma interaction. *Phys. Rev. Lett.* **93**, 135005 (2004).
- Kneip, S. *et al.* Bright spatially coherent synchrotron X-rays from a table-top source. *Nat. Phys.* **6**, 980–983 (2010).
- Corde, S. *et al.* Femtosecond X rays from laser-plasma accelerators. *Rev. Mod. Phys.* **85**, 1–48 (2013).
- Fourmaux, S. *et al.* Single shot phase contrast imaging using laser-produced Betatron x-ray beams. *Opt. Lett.* **36**, 2426–2428 (2011).
- Osterhoff, J. *et al.* Generation of Stable, Low-Divergence Electron Beams by Laser-Wakefield Acceleration in a Steady-State-Flow Gas Cell. *Phys. Rev. Lett.* **101**, 085002 (2008).
- Gonsalves, A. J. *et al.* Tunable laser plasma accelerator based on longitudinal density tailoring. *Nat. Phys.* **7**, 862–866 (2011).
- Nugent, K., Gureyev, T., Cookson, D., Paganin, D. & Barnea, Z. Quantitative phase imaging using hard X rays. *Phys. Rev. Lett.* **77**, 2961–2964 (1996).
- Paganin, D., Mayo, S. C., Gureyev, T. E., Miller, P. R. & Wilkins, S. W. Simultaneous phase and amplitude extraction from a single defocused image of a homogeneous object. *J. Microsc.* **206**, 33–40 (2002).
- Sidky, E. Y., Yu, L., Pan, X., Zou, Y. & Vannier, M. A robust method of x-ray source spectrum estimation from transmission measurements: Demonstrated on computer simulated, scatter-free transmission data. *J. Appl. Phys.* **97**, 124701 (2005).
- Popp, A. *et al.* All-optical steering of laser-wakefield-accelerated electron beams. *Phys. Rev. Lett.* **105**, 215001 (2010).
- Cipiccia, S. *et al.* Gamma-rays from harmonically resonant betatron oscillations in a plasma wake. *Nat. Phys.* **7**, 867–871 (2011).
- Pfeiffer, F. *et al.* High-resolution brain tumor visualization using three-dimensional x-ray phase contrast tomography. *Phys. Med. Biol.* **52**, 6923–6930 (2007).
- Yoneyama, A. *et al.* Phase-contrast X-ray imaging system with sub-mg/cm² density resolution. *J. Phys. Conf. Ser.* **425**, 192007 (2013).
- Saitoh, H., Fujisaki, T., Sakai, R. & Kunieda, E. Dose distribution of narrow beam irradiation for small lung tumor. *Int. J. Radiat. Oncol.* **53**, 1380–1387 (2002).
- ICRP. *ICRP Publication 110* (Elsevier Sci. Ltd166, 2009).
- Durbin, S. M., Clevenger, T., Graber, T. & Henning, R. X-ray phase-contrast imaging. *Philos. Trans. A Math. Phys. Eng. Sci.* **372**, 20130032 (2014).
- Zhou, S.-A. & Brahme, A. Development of phase-contrast X-ray imaging techniques and potential medical applications. *Phys. Med.* **24**, 129–148 (2008).
- Seres, E. & Spielmann, C. Time-resolved optical pump X-ray absorption probe spectroscopy in the range up to 1 keV with 20 fs resolution. *J. Mod. Opt.* **55**, 2643–2651 (2008).
- Durbin, S. M., Clevenger, T., Graber, T. & Henning, R. X-ray pump optical probe cross-correlation study of GaAs. *Nat. Photon.* **6**, 111–114 (2012).
- Chergui, M. & Zewail, A. H. Electron and X-ray methods of ultrafast structural dynamics: advances and applications. *Chemphyschem* **10**, 28–43 (2009).
- Bargheer, M. *et al.* Coherent atomic motions in a nanostructure studied by femtosecond X-ray diffraction. *Science* **306**, 1771–1773 (2004).
- Reagan, B. A. *et al.* Demonstration of a 100Hz repetition rate gain-saturated diode-pumped table-top soft x-ray laser. *Opt. Lett.* **37**, 3624–3626 (2012).
- Fattahi, H. *et al.* Third-generation femtosecond technology. *Optica* **1**, 45–63 (2014).
- Buck, A. *et al.* Absolute charge calibration of scintillating screens for relativistic electron detection. *Rev. Sci. Instrum.* **81**, 033301 (2010).
- Born, M. & Wolf, E. *Principles of Optics: Electromagnetic Theory of Propagation, Interference and Diffraction of Light* (Univ. Press, 1999).
- Burvall, A., Lundström, U., Takman, P. A. C., Larsson, D. H. & Hertz, H. M. Phase retrieval in X-ray phase-contrast imaging suitable for tomography. *Opt. Express* **19**, 10359–10376 (2011).
- Myers, G., Mayo, S., Gureyev, T., Paganin, D. & Wilkins, S. Polychromatic cone-beam phase-contrast tomography. *Phys. Rev. A* **76**, 045804 (2007).
- Gullikson, E. X-Ray Interaction With Matter. (2010). at <http://henke.lbl.gov/>.
- Mayo, S. *et al.* X-ray phase-contrast microscopy and microtomography. *Opt. Express* **11**, 2289–2302 (2003).

Acknowledgements

This work was supported by DFG through the Cluster of Excellence Munich-Centre for Advanced Photonics (MAP EXC 158) and TR-18 funding schemes, by EURATOM-IPP, and the Max-Planck-Society. S.S., M.B., and F.P. acknowledge financial support through the DFG Gottfried Wilhelm Leibniz program and the European Research Council (ERC, FP7, StG 240142). S.S. acknowledges the Technische Universität München graduate School for the support of her studies. P.T. acknowledges support from the ERC starting grant ‘OptImaX’ (#279753).

Author contributions

J.W., S.S., K.K., M.H., F.P. and S.K. designed and carried out the experiments. J.W., S.S. and K.K. performed the source characterization. S.S., M.B. and P.T. analysed the tomography data. J.W. and S.S. wrote the main part of the paper. F.P. and S.K. provided overall guidance and supervised the project. All authors discussed the results, reviewed and commented on the manuscript.

Additional information

Supplementary Information accompanies this paper at <http://www.nature.com/naturecommunications>

Competing financial interests: The authors declare no competing financial interests.

Reprints and permission information is available online at <http://npng.nature.com/reprintsandpermissions/>

How to cite this article: Wenz, J. *et al.* Quantitative X-ray phase-contrast microtomography from a compact laser-driven betatron source. *Nat. Commun.* **6**:7568 doi: 10.1038/ncomms8568 (2015).



This work is licensed under a Creative Commons Attribution 4.0 International License. The images or other third party material in this article are included in the article's Creative Commons license, unless indicated otherwise in the credit line; if the material is not included under the Creative Commons license, users will need to obtain permission from the license holder to reproduce the material. To view a copy of this license, visit <http://creativecommons.org/licenses/by/4.0/>